Fundamental Wind Tunnel Experiments on Tip-Fin Flutter

ICAS-94-9.4.4

Tetsuhiko Ueda, Tokuo Sotozaki and Kazuo Iwasaki

Airframe Division, National Aerospace Laboratory

Osawa, Mitaka-City, Japan

ABSTRACT

The baseline of H-II Orbiting Plane (HOPE) has a large fin at the tip of its cropped delta wing. During its mission which begins with vertical launch by H-II rocket and ends at horizontal landing, it will encounter severe circumstances for the airframe structure. One of the design issues of the structure is flutter as it has wings like airplanes. To investigate the fundamental characteristics of flutter for this configuration, a simple wing model with a vertical fin was made and tested in a low-speed wind tunnel. Present paper describes the vibration tests, wind tunnel experiments and the flutter calculations for this model. A unique tool for modal survey tests is also described.

Introduction

The unmanned reentry vehicle with wings is now planned as a space transportation system. The system is supposed to utilize the H-II rocket which recorded successfully its first flight in February 4, 1994. The plan is called HOPE project. The baseline of the vehicle has large fins at the tips of the main wings. The tip-fins have partial control surfaces for lateral control and stability, i.e. rudders. The stiffness of the main wing will be rigid enough since the wing takes rather thick structure if you consider the ordinary aircraft structure. The wing has, however, relatively large fins at the tip where the deflection of the elastic vibration becomes appreciable in lower fundamental frequency modes. It may bring about adverse unsteady aerodynamic forces for flutter. Furthermore, the flutter of this type of wings may include effects of the aerodynamic interference between non-coplanar lifting surfaces. It is not clear how accurately we can predict this type of flutter. The accuracy of flutter prediction can affect the design margin of the winged reentry vehicle. To investigate these problems, fundamental wind tunnel tests were conducted on a canti-levered tip-fin configuration wing. Prior to the wind tunnel tests, modal survey tests of the elastic model were carried out by using the newly synthesized measurement system which can automatically acquire the vibration data.

Wing Model

A canti-levered wing model with the tip-fin was tested in the 2m x 2m low-speed wind tunnel. The planform is shown in Figure 1. As can be seen in the figure, the model has a control surface of 30% partial span of the planform and the cant angle of 15° at 700mm in spanwise direction. The tip-fin is connected to the main wing with the attachment which has a folding angle of 75° . The root chord of the main wing is 1000mm in length. The model consists of separated balsa-wood airfoils and the spars of the aluminum alloy at a 40% chord line. Each airfoil has a 12% thickness ratio with straight camber. Stiffness distributions of the spars in design are shown in Figure 2 where the abscissa is a coordinate along the spar center. The rectilinear spikes at 0.787m in stiffness correspond to the attachment for the tip-fin. Three different kinds of supports were prepared for the rudder with removable mass balance. They were fixed, elastically supported by a torsion bar, and rotationally free with no constraint. For an elastically supported rudder, the deflection angle was monitored by the strain gage attached on the torsion bar during the wind tunnel tests. A small accelerometer was installed near the tip of the main wing to measure the vertical acceleration of the wing motion. Two strain gages are also attached on the spar at the wing root for bending and torsional deformations.

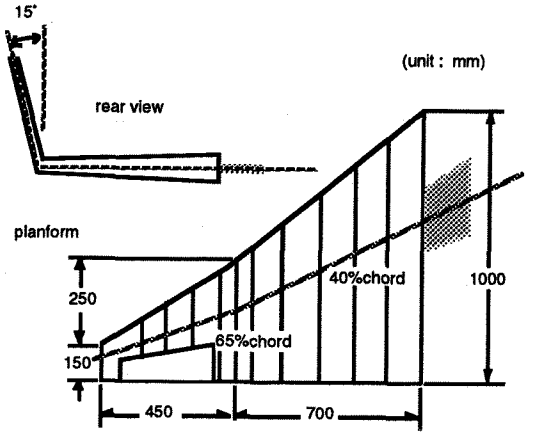

Fig.1 Planform. of the model

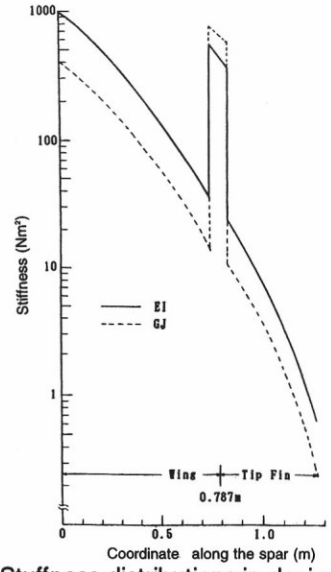

Fig. 2 Stuffness distributions in design of the model

Modal Survey

Dynamic Displacement Measurement System Modal survey tests for these models were carried out with a newly synthesized measurement system in NAL called Dynamic Displacement Measurement System. The system consists of a non-contact vibration sensor using laser Doppler effects, an industrial robot to support the sensor at specified positions, and the control computer for testing. The block diagram of the system is shown in Figure 3. Figure 4 shows a picture of the test setup with the measurement system. The main computer, which does not appear in the picture, controls the sequence of tests acquiring transfer functions between an excitation point and the sensing points on the structure. The non-contact vibration sensor measures normal velocities of the vibrating surface. Its operating distance is 100mm to 1000mm from the target. This type of sensor requires no focus depending on a distance, which is well matched for positioning by the robot. It can measure velocities from 20μm/s up to 1m/s at frequencies from 0Hz to 20kHz. The sensor covers a wide range of vibrations of the structure appearing in the aerospace fields. The laser

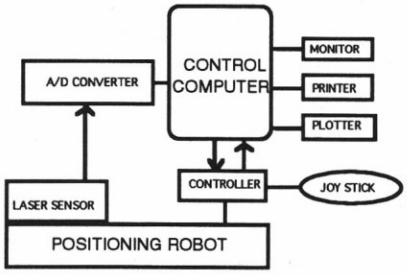

Fig.3 Block diagram of Dynamic Displacement Measurement Sysytem

beam of the sensor conforms to class II of BS4803, which is relevant for visual teaching. It is easy to teach positions of the sensor manually with a joy stick by adjusting a red spot of the laser beam on the structure surface. The robot has its own controller which is connected to the main computer through the RS232C interface and the discrete signal lines. The positioning robot has six axes each with a degree of freedom, enabling robot's motions to set the sensor in three-dimensional space aligned in an arbitrary direction. The longest arm of the robot is 2.5m in length. The accuracy of positioning directly affects the quality of the measurement data. The nominal margin of error was 0.2mm for repeating positions. A benchmark test performed with this system showed the standard deviation of the relative difference to be less than 0.02mm for fifty times repeating motions including six specified positions. For the data acquisition after the teaching, all you have to do is push the start key. The installed software program sequentially executes the position change of the sensor, generation of the burst random signals for exciters, acquiring the time history data of vibrations, and real time application of FFT to the acquired data to obtain transfer functions by communicating with the operator who goes through the quality of data to select target modes. For the model, forty-nine points on the corners of each airfoil segment were selected as measuring points. The setup parameters for the FFT were 30 times of averaging, 200Hz for the frequency range and the burst type of random forces for excitation. Only normal components of the deflection on the tip-fin portion were measured since they are essential for

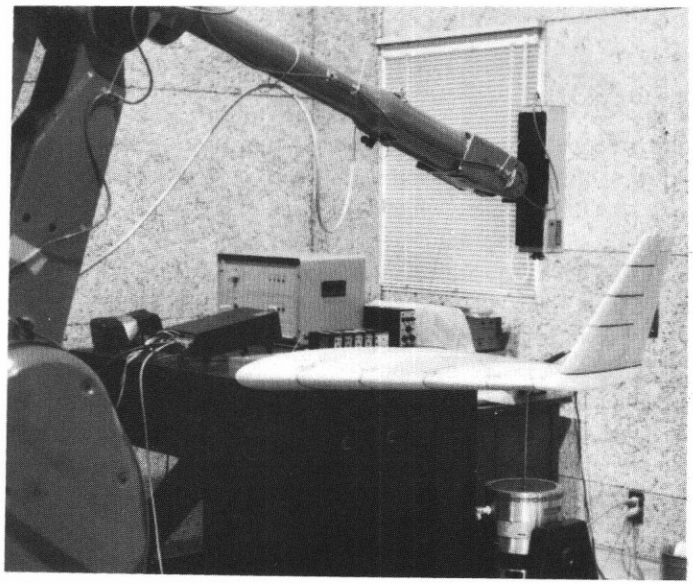
Fig.4 Test setup for modal survey tests

the flutter characteristics. With these conditions, it took only 80 minutes for one case of data acquisition, resulting in considerable time saving. Movements of the sensor to and from the tip-fin part were very smooth even though it had to rotate 75° for adjusting the sensor axis.

Dynamic characteristics of models To compare with the results of the modal survey tests, a mathematical model

simulating the actual model was formed by the finite element method with simple beam elements. The model is shown in Figure 5. Most of the nodal points are corresponding to the actual structure points of the airfoil segments. The properties of these elements of the spars and of airfoil segments are shown in Tables 1 and Table 2, respectively. Before the vibration analysis, the math model was tuned in accordance with the static load test on the spar. Since the

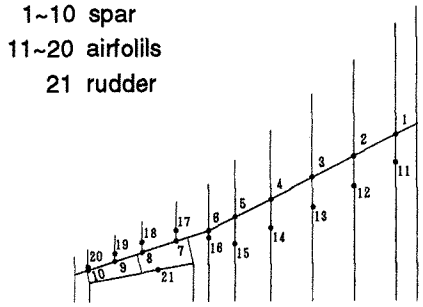

Fig.5 Math model by FEM with beam elements

node no.	w(gf)	Iy (gf mms²)
1	343.9	129.2
2	261.8	78.1
3	198.8	43.8
4	131.5	22.6
5	63.6	6.9
6	148.2	18.6
7	57.5	9.7
8	25.3	1.4
9	13.7	0.3
10	19.8	0.6

Table 1. Mass and moment of inertia of the spar

node no.	w(gf)	Iy (gf mms²)
11	733.8	5241.5
12	648.4	3353.6
13	566.2	2627.6
14	484.8	1838.7
15	389.1	420.6
16	215.4	343.1
17	87.7	56.1
18	49.7	17.6
19	36.9	8.9
20	29.9	6.8
21	166.3	28.8

Table 2. Mass and moment of inertia of the airfoils

stiffness distribution in Figure 2 is a design value, there would be some difference with the actual spar which was milled by the NC machine from the solid material. Static load tests were carried out with dead weights at the tip of the spars and the displacements were measured at several points. The stiffness of the math spars was corrected by multiplying factors determined from the static load test. They were 1.12 for bending and 1.03 for torsion of the wing spar, and 1.00 for bending and 0.90 for torsion of the tip-fin spar. Comparisons of measured displacements with those of the corrected math model are shown in from Figure 6a to Figure 6d. As can be seen in these figures, the math models of the spars were well adjusted to the measurements. Natural

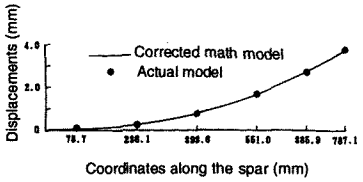

Fig.6a Bending deformation of main spar

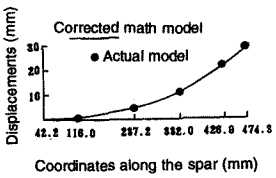

Fig.6b Bending defomation of tip-fin spar

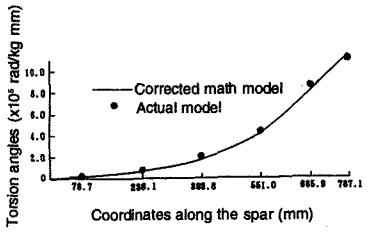

Fig.6c Torsional deflection of main spar

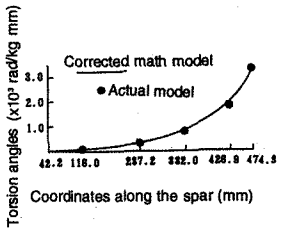

Fig.6d Torsional deflection of tip-fin spar

a) Rudder fixed

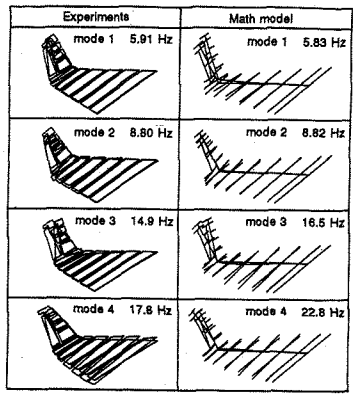

b) Elastic support

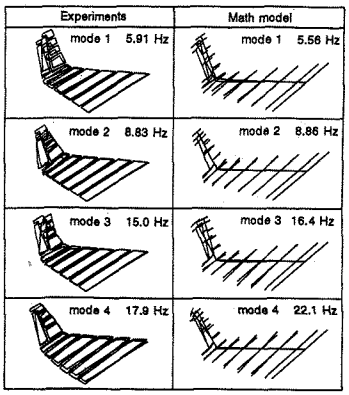

c) Rudder free

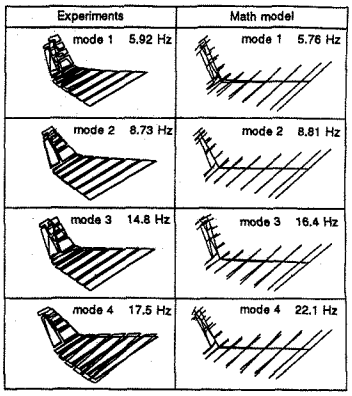

Fig.7 Comparisons between modal survey tests and analytical results by mathematical models

frequencies and corresponding eigen-modes were calculated with this math model and compared with the results of the modal survey tests. The comparisons were made in Figure 7' s. The figures show four lower fundamental modes for three different configurations comparing the test results with the analysis. The difference due to the rudder support is not much on either natural frequencies or vibration modes except for the small deflection of the rudder in the second modes. The natural frequency of the elastically supported rudder itself was 4.4Hz whereas the first bending mode of the whole model was 5.91Hz. The second modes were twisting modes of the main wing which may play an important role on flutter. The third and fourth modes are the second bending and the second torsion, respectively. Agreement between the math model and the actual model is good. Differences in natural frequencies for higher modes may come from the support structure of the rudder.

Wind Tunnel Experiments

Wind tunnel tests for flutter were conducted in Gust Wind Tunnel in National Aerospace Laboratory. The model was installed on the side wall of the tunnel. A schematic diagram of the flutter test is shown in Figure 8 and the model installed in the tunnel is shown in Figure 9. On the tunnel floor, a flutter stopper was furnished to prevent the model from destroying. It was a fence of mesh actuated by the air cylinder. During the tests, the sensor signals from the accelerometer and strain gages were analyzed and recorded with the real time multi-channel FFT analyzer. A laser sensor for dynamic displacements of the wing was also equipped on the floor 800mm apart from the wing surface. A video camera from outside of the wind-tunnel window was used to visually record the motion of the model. Utilizing the digital output of Pitot tube, the flow speed was displayed at the bottom of the tunnel window. It helped much to confirm the flutter critical speed from the record of VCR after the flutter tests. In the experiments, the flow speed was increased stepwise while watching the responses of the model to the flow turbulence until the flutter occurred. Autospectra of these responses with each vibration sensors were obtained when the flow speed was kept constant. Due to the good performance of the flutter stopper, the wing was able to survive violent flutters without any crucial damage for the structure.

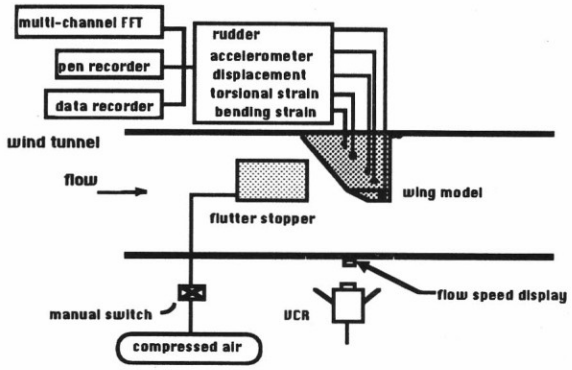

Fig.8 A schematic diagram of flutter tests

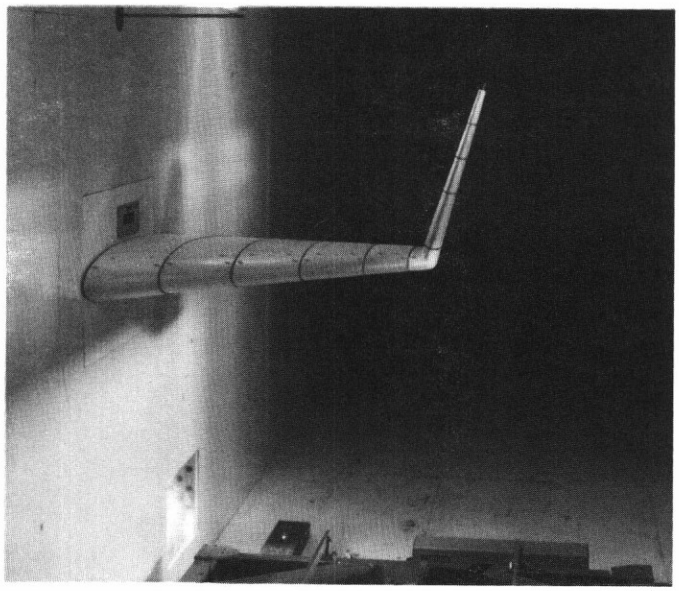

Fig.9 Model installed in the wind tunnel

Experimental Results

Flutter speeds could be clearly determined by the occurrence of flutter on the model. Five configurations were tested. They are the combinations of with or without mass balance, and three kind of supports for the rudder. For the fixed rudder, the case without mass balance was not tested because the removal of the mass balance was aimed to see the effect of mass balance only for the mobile control surfaces on a tip-fin. Flutter speeds and flutter frequencies obtained in the experiments are given in Table 3. The first case gives a result of the wing with the rudder fixed. The flutter showed typical bending-torsion flutter. The flutter frequency is 6.9Hz which falls between two natural frequencies of the fundamental bending and torsion modes. The second case shows a result of the configuration where the rudder was elasticity supported. The flutter speed becomes slightly higher than those in the case with the

Table 3. Flutter test results

case no.	mass balance	rudder support	flutter speed (m/s)	frequency (Hz)
1	yes	fixed	39.9	6.9
2	yes	elastic	41.6	6.6
3	no	elastic	11.0*	10.5*
4	yes	free	from 25.1 to 28.4*	8.0*
			42.0	6.7
5	no	free	~ 9 to more than 22*	9.7*

* mild flutter with limited amplitudes

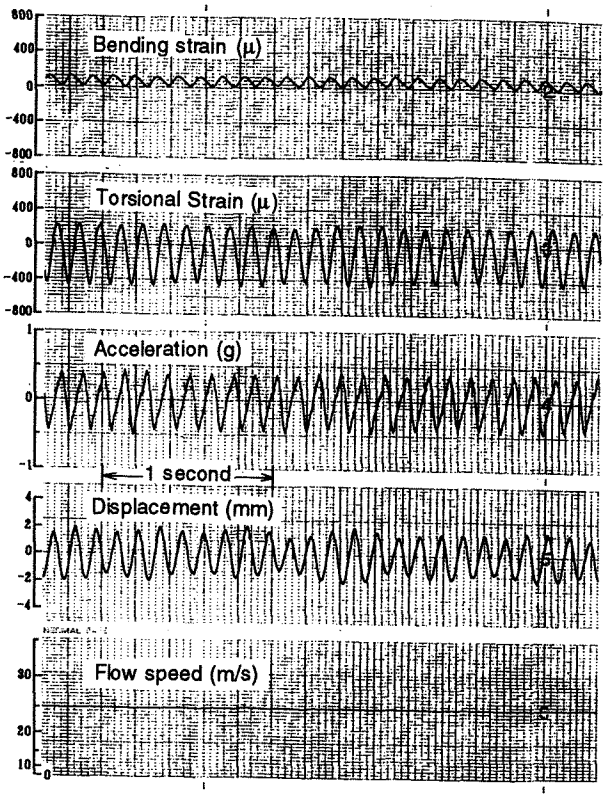

Fig.10 Time histroies of the mild flutter at 25.2m/s in Case 4

rudder fixed. But the difference was not much in speeds and frequencies between these two cases. The third case was for the wing with the elasticity supported rudder without any mass balance. The flutter began at a very low speed almost the start of the wind tunnel blowing. The frequency of this case was just above the second natural frequency of torsion. The fourth case was for the rudder without any constraint and showed somewhat interesting behavior of the flutter. The rudder had mass balance. At the flow speed of 25.1m/s, the wing suddenly started fluttering. The amplitudes of the oscillation were, however, not large and the oscillation was in a limit cycle with almost constant amplitudes. The time histories of this oscillation are shown in Figure 10. The records are bending strain, torsional strain, acceleration, vertical displacement of 67% chord at 608mm in the span coordinate, and the flow speed, respectively. Every vibration sensor showed the oscillation of 8.0Hz which is close to the second natural frequency of this configuration wing. As can be seen in the figure, the torsion of the main wing was dominant in this oscillation, which could be seen also in the visual observation of the flutter. The amplitudes of the rudder deflection seemed to be appreciable in the visual observation although there was no record of the rudder for this configuration. This mild flutter became attenuated and completely stopped at the speed of 28.4m/s. The flow speed continued to increase up to 42.0m/s where the violent flutter occurred. The last case was with neither constraint nor mass balance for the rudder. Again the flutter started at

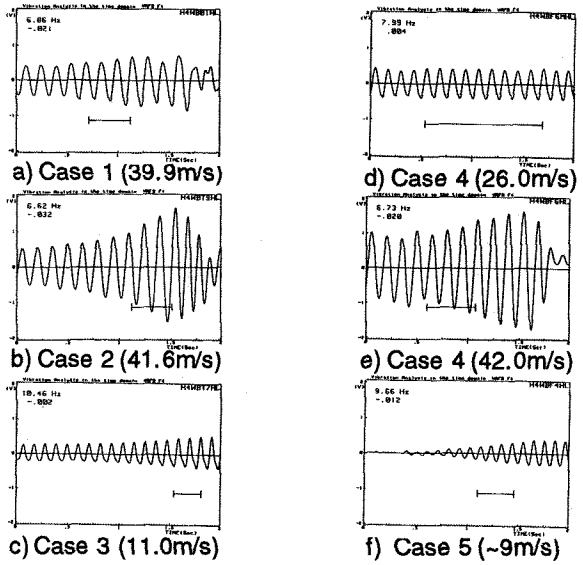

Fig.11 Flutter records

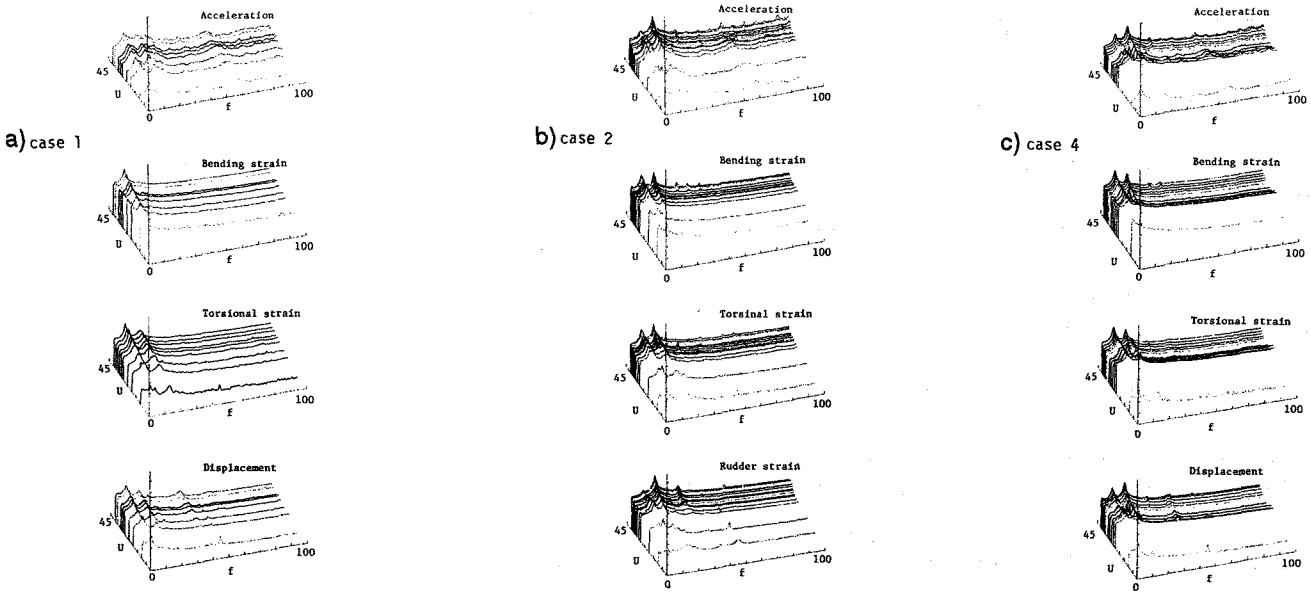

Fig.12 Variations of autospectra depending on speeds

very low speed of the beginning like in Case 3. Since the oscillation was limited within a small amplitude, the flow speed was increased up to 22m/s. During that time, no change could be seen. The frequency was similar to that of Case 3. These two cases without any mass balance clearly demonstrated the effects of the mass balance for control surfaces of this type of configuration as well. The time histories of the signal from the accelerometer are shown in Figure 11's at the onset of each flutter. These signals have been filtered by the digital IIR filter to determine the flutter frequencies of diverging oscillations. They were determined in the time domain with the VATREM method[1]. The bar symbols in those figures distinguish the data portions that were used for the calculation. The decaying end-parts of the oscillations correspond to the effects of the flutter stopper. As can be seen, it worked well. The digits shown below the frequencies in the corner are calculated negative damping values by the VATREM. Figures from 12a to 12c show the autospectra of signals from four different sensors varying with the flow speeds. They are from top to bottom the acceleration, bending strain, torsional strain, and the displacement, respectively. In Figure 12b, the bottom one is the output of torsional strain of the rudder support. The abscissa is the frequencies from 0Hz to 100Hz and the ordinate in a horizontal plane corresponds to the flow speed which was increased step by step during the wind tunnel operation. The scale spans from 0m/s up to 45m/s. In Figure 12a, we can see the coalescence of two lower natural frequencies going into flutter especially in the torsional strain autospectrum although it is not very clear. So is in Figure 12b. In this figure, it can be seen that the autospectrum of the rudder output is affected much by the second bending mode near the flutter speed. In Figure 12c, the peak at 8.0Hz which corresponds to the mild flutter clearly appears in the record of the flow speed of 27.0m/s for each spectrum. The peak disappears at the next flow speed of 29m/s.

Flutter analysis with math models

Flutter equation The flutter analysis was performed on these configurations with the math model which has been obtained from the FEM and the static and dynamic tests on the actual model structure. Five fundamental vibration modes were selected for the flutter calculation. For the elastically supported rudder, the rudder mode was included as the lowest frequency in the math model although the corresponding mode did not appear in the modal survey tests. This may be attributed to the ineffective direction of excitation for this vibration mode. For the rudder free configuration, an artificial rudder deflection mode was added in the analysis. If we denote with the vector $\mathbf{q}$ the amplitudes of the generalized coordinates for each mode by assuming the simple harmonic motion for the time variable, then the equilibrium equation at the flutter point becomes

$$-\omega^2 \boldsymbol{E}\boldsymbol{q} + \boldsymbol{\Omega}^2(1+ig)\boldsymbol{q} - \frac{1}{2}\rho U^2 \boldsymbol{A}\boldsymbol{q} = 0 \qquad (1)$$

where

$$\boldsymbol{E} = \begin{bmatrix} 1 & 0 & \dots & 0 \\ 0 & 1 & \dots & 0 \\ \vdots & \vdots & \ddots & \vdots \\ 0 & 0 & \dots & 1 \end{bmatrix}, \quad \boldsymbol{\Omega}^2 = \begin{bmatrix} \omega_1^2 & 0 & \dots & 0 \\ 0 & \omega_2^2 & \dots & 0 \\ \vdots & \vdots & \ddots & \vdots \\ 0 & 0 & \dots & \omega_M^2 \end{bmatrix}$$

$$\boldsymbol{A} = \begin{bmatrix} a_{11} & a_{12} & \dots & a_{1M} \\ a_{21} & a_{22} & \dots & a_{2M} \\ \vdots & \vdots & \ddots & \vdots \\ a_{M1} & a_{M2} & \dots & a_{MM} \end{bmatrix}$$

In Eq.(1), the matrices **E**, Ω^2, and **A** are the unit, the normalized stiffness and the aerodynamic matrices, respectively. The g assumes the structural damping. Diagonal elements of the stiffness matrix become equal to the natural frequencies when each assumed mode was normalized by the mass matrix. The factors in front of the aerodynamic matrix is the dynamic pressure of uniform flow. The aerodynamic matrix is an unsymmetric matrix with each element in complex values which are calculated by

$$a_{mn} = \int_S h_m \Delta p_n dS \qquad (2)$$

where h_m and Δp_n are the normal displacement of the m-th mode of the lifting surface S, and the unsteady lift distribution due to the n-th mode, respectively. The unsteady lift distribution is calculated as a function of the reduced frequency $k=b\omega/U$ where b is a representative length of the wing. Since the unsteady aerodynamic force due to the rudder deflection with interference effects of non-planar surfaces can be thought to play an important role in flutter of this model, the extended Doublet-Point Method for general configurations[2] was used for the aerodynamic calculations. Figure 13 shows the aerodynamic elements for the Doublet-Point Method used in the present calculation.

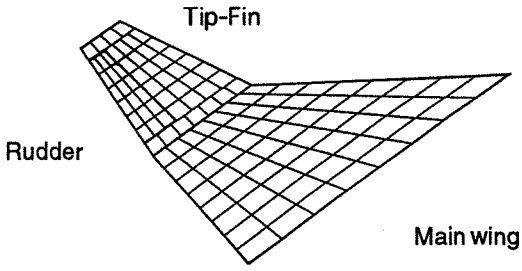

Fig.13 Aerodynamic elements of the Doulet-Point Method

Modifying the Eq.(1), we obtain the following complex eigen-value problem which leads to the conventional flutter calculation of the V-g method[3].

$$\frac{1+ig}{U^2}\boldsymbol{q} = \boldsymbol{\Omega}^{-2}\left[\frac{1}{2}\rho \boldsymbol{A} + \left(\frac{k}{b}\right)^2 \boldsymbol{E}\right]\boldsymbol{q} \qquad (3)$$

The case of rudder free If the rudder has no constraint about its rotation, the stiffness matrix becomes singular with a zero frequency associated with the rudder deflection mode. In this case, we cannot obtain the inverse matrix appearing in Eq.(3). Suppose this mode is the last M-th mode of the generalized coordinates. Then the aerodynamic matrix term in Eq.(1) can be rewritten as

$$Aq = \left[\begin{array}{c|c} A' & A_{1M} \\ \hline A_{M1} & a_{MM} \end{array}\right] \begin{pmatrix} q' \\ q_M \end{pmatrix} \tag{4}$$

where the primes indicate the quantities with the (M-1) degrees of freedom. Eliminating the M-th generalized coordinate, we obtain the matrix eigenvalue problem with the dimension of (M-1) by (M-1), instead of Eq.(3) as

$$\frac{1+ig}{U^2} q' = \Omega'^{-2} \left[\frac{1}{2}\rho \left\{ A' - \frac{\frac{1}{2}\rho A_{1M} A_{M1}}{\frac{1}{2}\rho a_{MM} + \left(\frac{k}{b}\right)^2} \right\} + \left(\frac{k}{b}\right)^2 E' \right] q' \tag{5}$$

In the aerodynamic calculation for the rudder, the deflection δ_r should be normalized by

$$\delta_r = (I_r)^{-\frac{1}{2}} \tag{6}$$

where I_r is the moment of inertia of the rudder about its hinge. In the actual computation, Eq.(3) can be utilized by substituting a very small frequency for the rudder mode. Example computation showed that the difference between Eqs.(3) and (5) became negligible if we used 1% of the smallest value of the other components. We used Eq.(3) for the results of this analysis. It should be noted here that the rudder frequency is associated with almost constant reduced frequencies for different U's since its restoring force can be thought proportional to the dynamic pressure of the uniform flow.

Analytical results

Flutter calculations were carried out for the three configurations of different rudder supports with the mass balance. For the stiffness matrix, the results of the modal survey tests were substituted in lieu of the vibration analysis with the math models. The structural damping g was set to zero in the present calculations. The correction factor of 0.85 for the aerodynamic forces of control surfaces[9] was introduced as is known for the lifting surface theory. Figure 14 shows a result of the U-g plots and frequency changes of the wing with rudder constraint. As the flow speed U increases, the second branch goes into the unstable region of positive g. The frequency change implies that the flutter is caused by the coupling of the lower two modes which are fundamental bending and torsion. The calculation gives the flutter speed as 36.8m/s whereas the experimental flutter boundary was

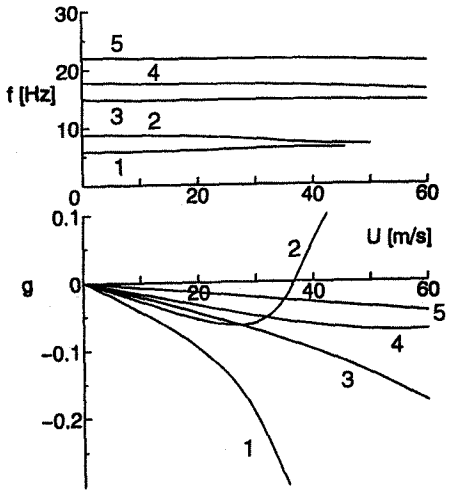

Fig.14 U-g plots for Case 1

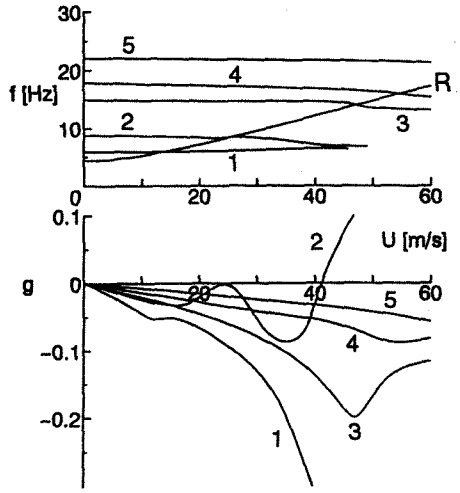

Fig.15 U-g plots for Case 2

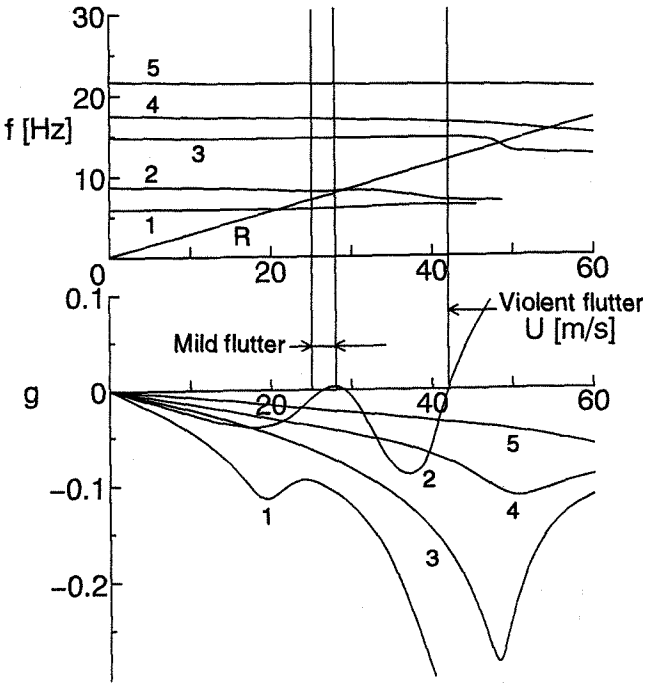

Fig.16 U-g plots for Case 4

39.9 m/s. The difference is 7.8% in the conservative side. The flutter frequency of this case is 7.3Hz which is 5.8% higher than that in the experiment. In this case, the flutter characteristics seems very typical as was in the experimental result. Figure 15 shows a calculated result of the wing with the elastically supported rudder, which corresponds to Case 2 in Table 3. Since this wing has a degree of freedom of rudder deflection, the rudder branch exists in the frequency curve. When U=0, the frequency coincides with its natural frequency. As the flow speed increases, it also increases almost linearly depending on the flow speed U with some influence on the other natural frequencies. This branch does not appear in the U-g plots because of its large negative g values. Although the damping of the second branch becomes worse around the speed of 25m/s, it gains again more damping until it finally penetrates the boundary at 41.1m/s. In the experiment, flutter occurred at 41.6m/s. As a result, rudder motion raised the flutter speed about 12%. This tendency was seen in the experiments, too. It was observed that the rudder was oscillating as if it would absorb the flutter occurrence of the main wing. The calculated flutter frequency is 7.0Hz whereas the experimental frequency was 6.6Hz. The calculated result for the peculiar flutter case was shown in Figure 16. The configuration corresponds to Case 4 in Table 3. In this figure, experimental speeds are also shown with arrow symbols. Similar to Figure 15, the frequency of the rudder mode increases as the flow speed increases. The second branch in U-g plots goes into the unstable region in the range from 26.0m/s to 28.4m/s in speeds with almost constant frequencies from 8.1Hz to 8.2Hz. It becomes stable again for higher speeds. This branch finally reaches the flutter where it coalesces with the first bending mode at 41.9m/s with the frequency of 6.9Hz. The behavior explains well the experimental results. Although the linear theory is not able to analyze the limit cycle oscillation, it can be said that the mild flutter corresponds to the small positive damping in that region. Further, this mild flutter was induced by the rudder motion of which frequency becomes very close to the second natural frequency of the wing. To confirm this, the flutter modes were calculated at the flutter points of 26.0m/s and 41.9m/s. The results were shown in Figure 17. Each shows rear views in the steps by 1/8 period. As can be seen in the figure, the flutter motion of the mild flutter involves much deflection of the rudder in contrast with the flutter at 41.9m/s.

Table 4. Comparison of the analysis and experiments

case no.	flutter speeds		flutter frequencies	
	analysis (m/s)	error	analysis (Hz)	error
1	36.8	-7.8%	7.3	+5.8%
2	41.1	-1.2%	7.0	+6.1%
4	26.0~28.7	+5.6~3.6%	8.1~8.2	+1.3~2.5%
	41.9	-0.2%	6.9	+3.0%

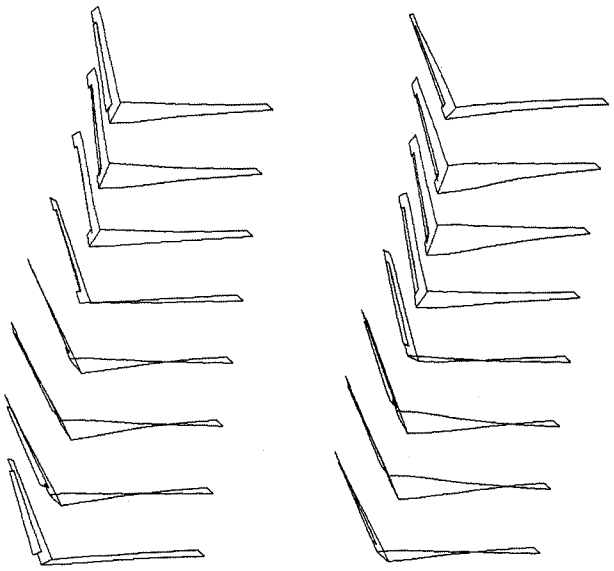

a) mild flutter at 26.0m/s b) flutter at 41.9m/s

Fig.17 Flutter modes

The results are summarized in Table 4 comparing the analysis and the experiments. It shows an excellent agreement.

Concluding remarks

Fundamental wind tunnel experiments for flutter of a tip-fin configuration wing and the flutter analysis were conducted. Modal survey tests on the model were successfully carried out by Dynamic Displacement Measurement System which enables us to obtain transfer functions in an automated sequence. In the wind tunnel tests, the mild flutter was observed in a certain range of flow speeds when the rudder was rotationally free with mass balance. The flutter was caused by the coalescence of rudder motion and torsion of the main wing. Flutter calculations using the non-planar Doublet-Point Method for unsteady aerodynamic forces clearly demonstrate the phenomena with good accuracy.

REFERENCES

1. T. Ueda and K. Iwasaki, "Vibration Analysis in the Time-Domain by the Real Eigenvalue Method", AIAA Paper 87-0945, 1987.
2. T. Ueda, "Unsteady Aerodynamic Calculations for General Configurations by the Doublet-Point Method", NAL TR-1101T, 1991.
3. E. H. Dowell, A modern course in aeroelasticity, Sijthoff & Noordhoff, Alphen aan den Rijn, 1978.
4. I. Abel, B. Perry III and J. R. Newsom, "Comparison on Analytical And Wind-Tunnel Results for Flutter and Gust Response of a Transport Wing with Active Controls", NASA TP 2010, 1982.